Materials Research. 2026; 29: e20250573
DOI: https://doi.org/10.1590/1980-5373-MR-2025-0573

Role of Particle Grading on Slurries Curing, Mechanical Properties, and Light Transmittance of DLP-Processed Zirconia Ceramics

Hengchang Cui*[a], *Xia Zhang*[a], *Zhuoqun Han*[a], *Guopu Shi*[a], *Ling Li*[a]

[a]*University of Jinan, School of Materials Science and Engineering, Nanxinzhuang West Road, 336, 250022, Jinan, Shandong, China.*

Received: July 31, 2025; Revised: October 16, 2025; Accepted: November 29, 2025

3D printing technology enables the fabrication of complex-structured ceramic components, while Digital Light Processing (DLP) offers superior precision and faster printing speeds. This study prepared zirconia slurries with 45 vol% solid loading using particle gradation technology with different coarse-to-fine powder ratios, systematically investigating the effects of particle size distribution on slurry rheological properties, curing characteristics, and sintered body performance. Experimental results demonstrated that the 80:20 ratio exhibited optimal comprehensive performance. At this ratio, the zirconia slurry showed a viscosity of 4.94 Pa·s at 50 s^{-1} shear rate and achieved a curing depth of 165 μm at 120 mJ/cm^2 energy density. This originates from increased interparticle surface contact due to fine particle incorporation, which enhances steric hindrance effects and consequently reduces powder-resin matrix fluidity, while the enlarged specific surface area significantly improves ultraviolet (UV) light absorption efficiency. After sintering at 1550°C, preferential diffusion of fine particles into grain boundary gaps promoted sintering densification, concurrently inhibiting abnormal grain growth and reducing light-scattering defects, thereby achieving simultaneous improvement in both mechanical properties and optical translucency.

Keywords: *Digital Light Processing, Zirconia ceramic, Particle grading, Rheological properties, Curing characteristics.*

1. Introduction

Zirconia (ZrO_2) is one of the most important ceramics due to its excellent mechanical and functional properties, including high flexural strength, stiffness, hardness, wear resistance, chemical stability, and biocompatibility[1,2]. For instance, zirconia has been widely used in medical and related fields, such as dental implants (e.g. , all-ceramic crowns)[3,4], and in the field of new energy materials, it serves as a key electrolyte material for solid oxide fuel cells[5]. With the continuous advancement of societal demands, there is a progressive increase in requirements for zirconia ceramics that integrate both superior comprehensive properties and sophisticated structural designs. Conventional manufacturing methods, such as mold pressing and machining, face considerable challenges in producing complex-shaped and functionally integrated zirconia components such as intricate mold design, high manufacturing costs, prolonged production cycles, machining difficulties[6,7]. Due to these limiting factors hindering the broader application of zirconia ceramics.

3D printing technology has successfully overcome the limitations of conventional formative manufacturing and subtractive processing methods. By integrating three core technological modules—mechanical design, digital control, and materials R&D—this approach achieves rapid manufacturing capabilities[8,9], 3D printing facilitates the fabrication of highly intricate structures that are unattainable through traditional manufacturing techniques. Owing to its high material efficiency, shortened production cycles, and material versatility, AM has gained prominence in aerospace, defense, energy, biomedical, automotive, and high-end jewelry industries[10-12].Among various 3D printing technologies, Digital Light Processing (DLP), a vat photopolymerization-based method, has attracted significant attention for advanced ceramic fabrication due to its outstanding advantages[13-16]. DLP not only overcomes the constraints of conventional ceramic processing but also produces components with excellent surface finish and dimensional precision[17-19]. As demonstrated by Su et al., zirconia ceramics fabricated via DLP exhibited remarkable properties after sintering at 1500°C, achieving an average relative density of 97.33%, Vickers hardness of 12.55 GPa, and maximum flexural strength of 411.33 MPa[20].

Although digital light processing (DLP) technology has been successfully applied in polymer and metal dental restorations, its application in dental ceramics remains in the early stages. Current research on zirconia additive manufacturing primarily focuses on achieving mechanical properties comparable to those of conventionally processed ceramics, while largely neglecting the crucial parameter of translucency. The commonly used 3 mol% yttria-stabilized tetragonal zirconia polycrystals (3Y-TZP) exhibit poor translucency in additive manufacturing, whereas 5 mol% yttria-partially stabilized zirconia (5Y-PSZ), while demonstrating higher translucency, shows inferior mechanical properties compared to 3Y-TZP[21-24].

*e-mail: quanzhongliling@bjut.edu.cn
Associate Editor: Celso Santilli.
Editor-in-Chief: Luiz Antonio Pessan.

Consequently, achieving simultaneous improvement in both translucency and mechanical properties has become a core challenge in zirconia additive manufacturing.Theoretically, optimizing particle gradation to enhance packing density may improve overall material performance. Shi successfully enhanced the mechanical properties of SiC components by studying the particle size distribution of silicon carbide[25]. However, variations in powder particle size significantly affect both the cure depth and viscosity of the slurry[26]. Zhao's investigation on the effects of Si_3N_4 ceramic particle gradation on slurry performance demonstrated that increasing the mass ratio of fine particles elevates slurry viscosity while reducing cure depth[27]. Similarly, Hu et al.'s investigation on the photopolymerization behavior of silicon carbide (SiC) powders revealed that larger particles exhibit reduced optical absorbance, thereby enabling greater cure depth[28].Currently, research on zirconia (ZrO_2) slurries mainly concentrates on single-sized powder systems, while systematic studies on particle gradation optimization for photocurable ZrO_2 slurries and their resulting properties remain remarkably scarce.

In this study, we established a particle gradation system by incorporating a small amount of 90 nm zirconia powder into 500 nm zirconia powder. While systematically investigating its effects on slurry properties and mechanical performance, we concurrently examined the influence of particle gradation on optical translucency. Through comprehensive analysis of the gradation system's impact on slurry characteristics, as well as the evolution of mechanical properties and translucency after sintering, the optimal gradation ratio was determined within the experimental composition range. Ultimately, the particle gradation technique successfully achieved simultaneous enhancement of both mechanical properties and translucency in zirconia ceramics.2. Experimental procedures.

2.1. Material preparation

Two types of ZrO_2 powders were used, including D01 (D_{50} = 500 nm, 3Y-TZP, Shandong Guangyin, China) and D02 (D_{50} = 90 nm, 5Y-PSZ, Tosoh, Japan). The photosensitive resin was propoxylated trimethylolpropane triacrylate (PO3TMPTA), which provided the cured layers with excellent toughness and strength. The dispersant, X-100 (Jintenlong, China), was employed to ensure better powder distribution in the resin. Polypropylene glycol 400 (PPG 400, Aladdin, China) was added as a plasticizer to facilitate the debinding process.

2.2. Preparation of the ZrO_2 powders

The mass ratio of ZrO_2 powders was determined according to the data in Table 1. The coarse-to-fine powder mass ratios were set at 100:0, 95:5, 90:10, 80:20, and 70:30, respectively.

Table 1. Gradation ratios of ZrO_2 powder.

Samples	D01:D02
D1	100:0
D2	95:5
D3	90:10
D4	80:20
D5	70:30

2.3. Preparation of DLP-compatible ZrO_2 slurry

PO3TMPTA and PPG-400 were mixed in a 6:4 ratio, with 1.5% photoinitiator TPO and 0.5% photoinitiator Irgacure 819 added to the blended resin. A dispersant (4 wt% relative to powder mass) was introduced. The mixture was then heated in an ultrasonic homogenizer at 40-50°C for 10 minutes to dissolve particulates, yielding the prepared photosensitive resin. The ZrO_2 powder was sequentially added to the photosensitive resin in three batches at a 2:2:1 ratio. After each powder addition, homogenization was performed using a homogenizer to ensure uniform dispersion. This stepwise addition method facilitates powder dispersion under high solid loading conditions, preventing agglomeration and mixing difficulties associated with single-batch powder incorporation. Ultimately, zirconia slurry with 45 vol% solid loading was obtained through this sequential homogenization process.

2.4. Printing and forming green bodies using DLP printing

Ceramic stereolithography experiments were conducted using a customized DLP printer (self-developed equipment, Shandong Industrial Ceramic Research & Design Institute) employing a bottom-up design. The system utilized 405 nm ultraviolet light for curing with a set printing layer thickness of 50 μm. To evaluate the microstructure and mechanical properties, standard test bars measuring 3 mm × 4 mm × 36 mm and circular discs with a radius of 15 mm and a thickness of 1 mm were printed, with scaling adjustments made during printing based on shrinkage. Each group consisted of 10 test bars and 5 discs.

2.5. Debinding and sintering process design

The pressureless thermal debinding-sintering process was employed, wherein the debinding stage followed a temperature program established based on the thermal decomposition characteristics curve obtained through thermogravimetric analysis (TGA) of green bodies, ensuring effective removal of organic components from the specimens. The temperature was raised from room temperature to 500 °C at a rate of 1 °C/min, with dwell times of 2 hours at 200 °C, 365 °C, and 405 °C to eliminate organic components. Finally, sintering was conducted at 1500-1600 °C (heated from room temperature at 3°C/min) with a 2-hour holding time.

2.6. Characterization techniques

The viscosity of the slurries was measured using a rheometer (MCR 92, Anton Paar, Austria) to systematically investigate the influence mechanisms of powder particle size distribution and blending ratios on the viscous behavior of the slurries. Microstructural characterization of specimens prepared under different sintering temperatures and powder ratios was performed using a scanning electron microscope (SEM, Sigma 300, Zeiss, Germany).Phase analysis was performed using an X-ray diffractometer (XRD, D8 Advance, Bruker, Germany). XRD measurements were conducted with Cu Kα radiation over a 2θ range of 10° to 80°.The density of sintered samples was calculated using the Archimedes principle drainage method to determine the influence of different graded powders on the sintering density of ZrO_2.

The mechanical properties were evaluated using a universal testing machine (Shimadzu AGIS 30 KN, Japan) to determine the three-point flexural strength and elastic modulus of standard specimens (4 mm × 3 mm × 36 mm), with Vickers hardness measurements conducted on a hardness tester (Shanghai Shangcai HRS-150). All tests were performed in accordance with ASTM C1161 standards.

The transmittance of disc-shaped samples was measured using a full-range ultraviolet spectrophotometer (UV-3600 Plus, Shimadzu, Japan).

3. Results and Discussion

3.1. Experimental principle

According to the Furnas model, in a particle gradation system, when the diameter ratio of coarse to fine particles exceeds 5:1 (500nm/90nm≈5.6), fine particles can effectively fill the interstices formed by coarse particle packing. As shown in Fig. 1, rational proportioning of differently sized particles enables complete filling of interparticle voids, simultaneously enhancing material density while reducing light scattering. This optimized particle size distribution results in comprehensive improvement of material properties.

3.2. Slurry rheology

The slurry exhibits shear-thinning behavior, as shown in Fig. 2. The optimal dispersion effect is achieved when the dispersant dosage is 4%. Fig. 3 reveals that the slurry with the smallest particle size (70:30) shows the highest viscosity. As the particle size increases from 100:0 to 70:30, the viscosity of the slurries progressively rises, measuring 2.32 Pa·s, 3.46 Pa·s, 3.67 Pa·s, 4.94 Pa·s, and 8.24 Pa·s,at a shear rate of 50 s^{-1}. This trend can be attributed to the reduced surface contact between larger particles, which weakens interparticle steric hindrance and enhances flowability between the powder and resin. These observations align with the findings reported by Olhero[29].

3.3. Curing characteristics

The photopolymerization process constitutes the core and most critical step in the overall printing procedure. The cure depth determines the settable range for the single-layer printing thickness, with greater cure depths enabling broader setting ranges. The specific testing method involved coating the ceramic photosensitive slurry onto a glass slide, which was then positioned at the center of the vat in a 3D printer. Through parameter configuration of the 3D printer, the exposure intensity was maintained constant (30 mW/cm^2) while varying the exposure time to cure the slurry on the glass slide. After exposure completion, the cured single-layer sample was extracted, cleaned with alcohol, and the single-layer cure thickness was measured using a digital spiral micrometer, with five measurements taken per sample group. Fig. 4(a) systematically compares the photopolymerization characteristics of zirconia slurries with different mixing ratios.

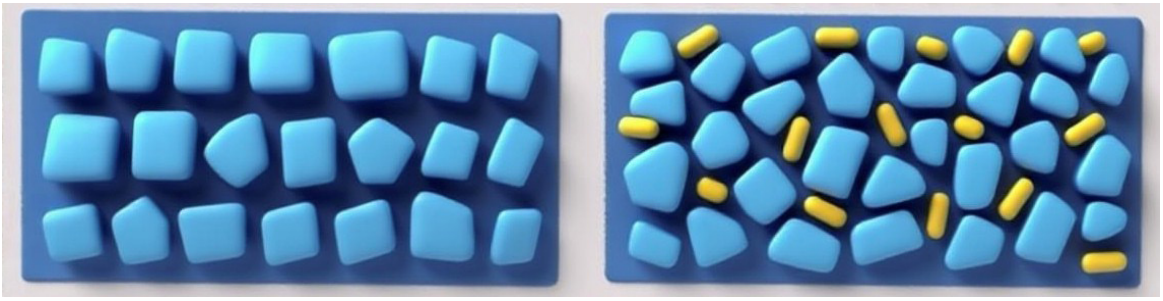

Figure 1. Schematic illustration of particle gradation mechanism.

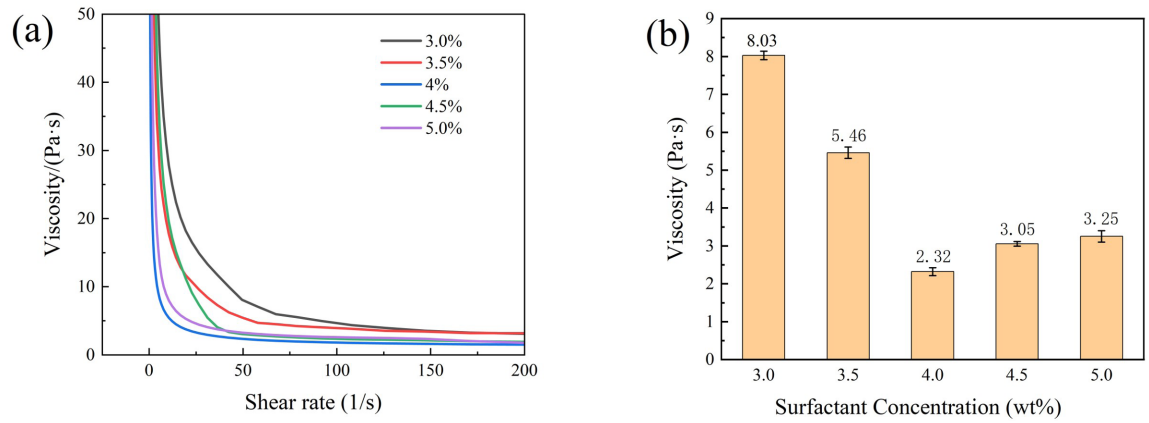

Figure 2. (a) Viscosity-shear rate curves of ceramic slurries with different dispersant contents, (b) viscosity.

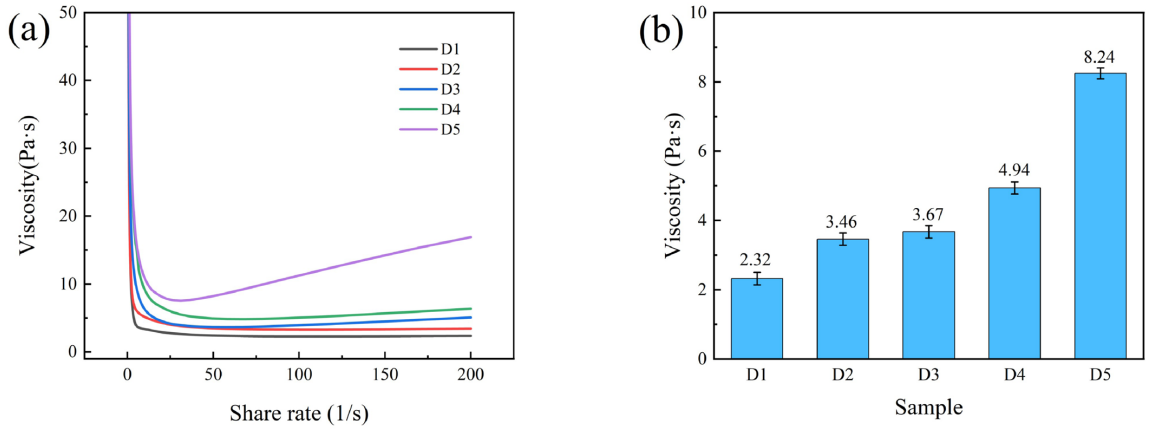

Figure 3. (a) Viscosity-shear rate curves of zirconia slurries with different formulations, (b) viscosity values at a shear rate of 50 s^{-1}.

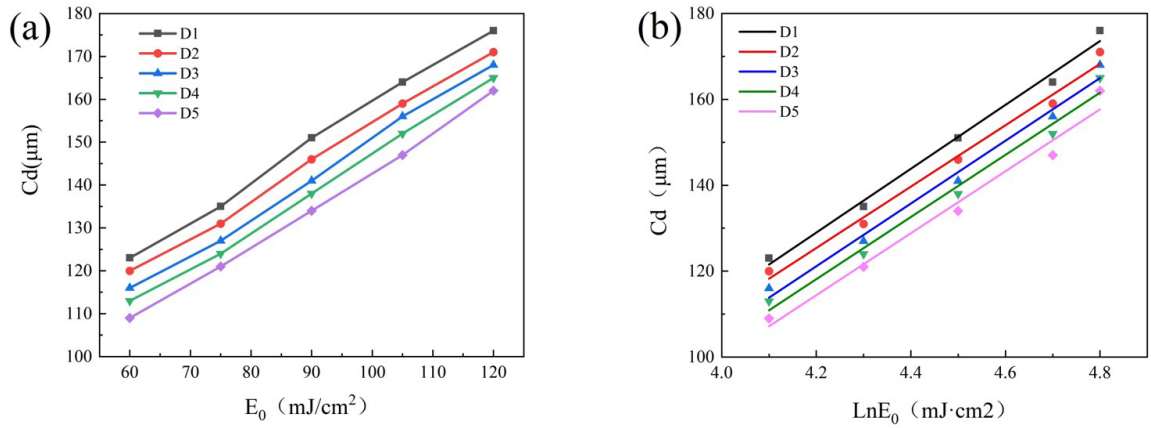

Figure 4. (a) Curing depth curves of zirconia slurries with different formulations, (b) Lambert-Beer plots.

Analysis of the relationship between cure depth and exposure energy density via Digital Light Processing (DLP) revealed that under identical exposure durations, the D5 (70:30) slurry exhibited the minimum cure depth (162 μm), while the D1 (100:0) slurry demonstrated the maximum curing performance (176 μm). At an exposure energy density of 120 mJ/cm^2, the cure depths of slurries from D1 (100:0) to D5 (70:30) showed a decreasing trend, with measured values of 176±4 μm, 171±1 μm, 168±2 μm, 165±3 μm, and 162±2 μm, respectively. As the powder particle size decreases, the absorbance increases and the cured thickness diminishes. This occurs because finer powder particles possess a larger specific surface area (SSA). The increased SSA enhances ultraviolet (UV) light absorption, consequently reducing the cure depth of the zirconia slurries[30,31].

The characteristic curve presented in Fig. 4(b) was derived by correlating measured incident energy densities with corresponding cure depths of the slurries, following the fundamental principles of the Lambert-Beer law[32]:

$$C_d = D_p \ln\left(\frac{E_0}{E_d}\right) \quad (1)$$

In the equation, Cd represents the cure depth, Dp denotes the penetration depth, E0 is the incident energy, and Ed stands for the critical exposure energy. Analytical results demonstrate that the gradual increase in critical curing energy required for slurry formulation is directly caused by the reduction in powder particle size, which is consistently verified by the cure depth test results.

The UV absorption mechanism illustrated in Fig. 5 demonstrates that the significant attenuation of light intensity results from increased particle density per unit thickness, which induces multiple light absorption events within the slurry and consequently leads to a marked decrease in penetration depth.

3.4. Determination of thermogravimetric analysis and sintering regimen

As shown in Fig. 6, the debinding process is employed to remove organic components from the green body, followed by pressure-assisted sintering to obtain dense and high-strength ZrO_2 samples. The thermogravimetric curves reveal that organic removal occurs primarily in three distinct temperature stages:The first stage from 167 to 262°C involves decomposition and volatilization of small-molecule organics, resulting in

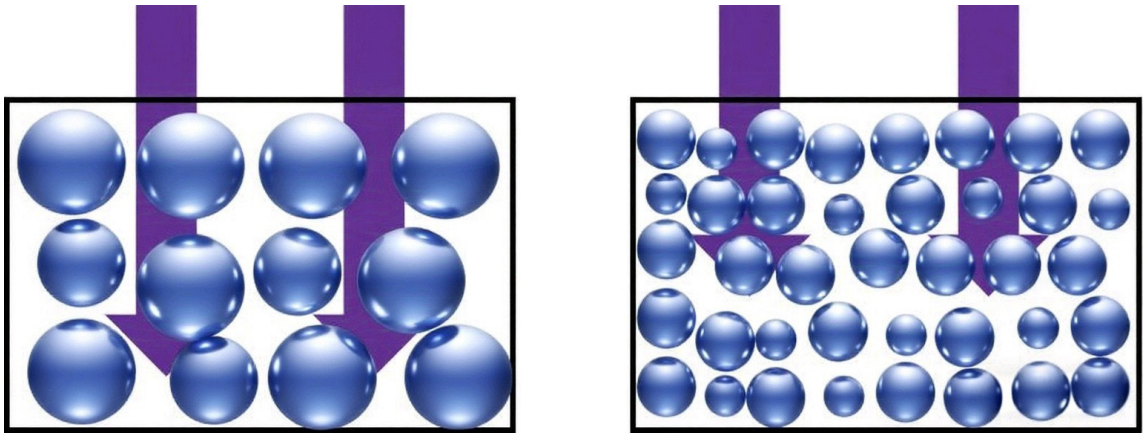

Figure 5. Mechanism schematic of UV absorption.

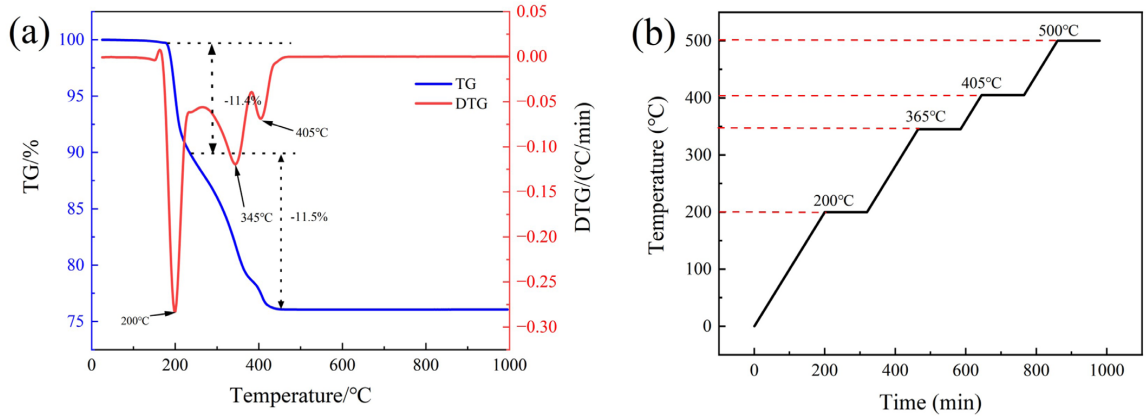

Figure 6. (a) TG-DTG curves of zirconia green bodies, (b) debinding profile curves.

approximately 11.4% mass loss of the green body while forming pore channels. This stage maintains a heating rate of 1°C/min with a 2-hour isothermal hold at 200°C.Subsequently, the second stage between 262 and 380°C and the third stage from 380 to 500°C exhibit successive decomposition and volatilization of organics, leading to significant combined mass loss of ~11.5%. To prevent cracking and defects in the green body during these critical stages[33], the process maintains consistent heating rates of 1°C/min with 2-hour isothermal treatments at 345°C and 405°C respectively, as systematically illustrated in the debinding schedule presented in Fig. 6b.

As shown in Fig. 7(a), the monoclinic phase disappears after particle gradation, indicating that fine powders form nanoscale intergranular phases which suppress the tetragonal-to-monoclinic (t→m) phase transformation. Meanwhile, Fig. 7(b) reveals that sintering temperature induces no significant alterations in diffraction peak positions or intensities, confirming its negligible impact on the phase structure of ceramics.

3.5. Characterization of zirconia ceramic properties

The densification degree, pore structure characteristics, and phase transformation kinetics of ceramic materials are all significantly governed by the particle size distribution (PSD) of the raw powders, consequently, the mechanical performance of ZrO_2 ceramics is critically determined. The ZrO_2 test bars fabricated via Digital Light Processing (DLP) technology underwent debinding and sintering in the aforementioned system. Five distinct ZrO_2 ceramic specimens with different powder formulations were prepared, and their relevant properties were comprehensively characterized.

Fig. 8 presents the fracture surface microstructural characteristics of ZrO_2 samples with different particle size distributions. SEM analysis reveals that the incorporation of fine particles reduces the average grain size, improves size distribution uniformity, and concurrently decreases interparticle porosity in zirconia ceramics during sintering.

Comparative surface groove SEM micrographs in Fig. 9 demonstrate that the particle distribution after gradation becomes more uniform, effectively filling interparticle voids.

The fracture surface microstructure of ZrO_2 samples sintered at different temperatures, as presented in Fig. 10, demonstrates through SEM analysis that increasing sintering temperature promotes grain growth while significantly reducing interparticle porosity.Within the 1400-1500°C range, grains exhibit incomplete development; when the temperature rises to 1550°C, complete grain growth is achieved; further increasing to 1600°C results in abnormal grain growth.

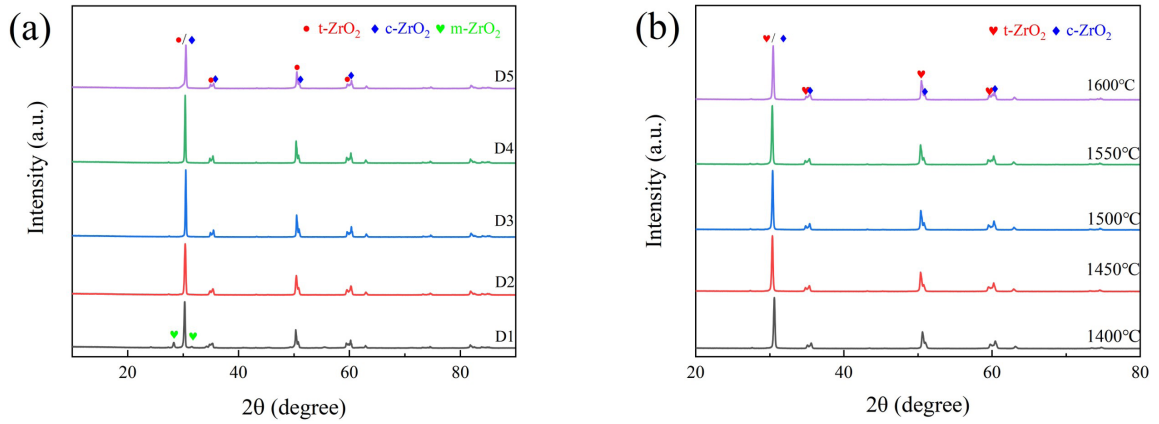

Figure 7. XRD patterns of ZrO_2 samples: (a) with varying particle size ratios sintered at 1550°C, (b) D4 (80:20 ratio) samples at different sintering temperatures.

Table 2. Comparison of properties for ZrO_2 ceramics with different ratios sintered at 1550°C.

Num	Curing thickness (μm, 120 mJ/cm^2)	Viscosity (Pa·s)	Elastic modulus (GPa)	Flexural strength (MPa)	Density (g/cm^3)	Vickers hardness (GPa)	Transmittance (%)
D1	176	2.32	195	709	6.01	14.0	34.7
D2	171	3.46	198	754	6.05	14.1	38.5
D3	168	3.67	204	805	6.07	14.2	42.6
D4	165	4.94	208	823	6.08	14.4	48.9
D5	162	8.24	189	654	5.86	14.1	44.1

Fig. 11 presents the density and relative density measurements of sintered ZrO_2 ceramics (n=5). It can be observed that as the average particle size of the powder decreases, the material density first increases and then decreases. The D4 (80:20) sample demonstrates the highest degree of densification, achieving a relative density of 99.67%. In contrast, the density reduction observed in the D5 (70:30) samples is attributed to their excessively high slurry viscosity, which compromises printing quality and ultimately leads to diminished density in the corresponding sample set.

Fig. 12 presents the mechanical properties of five samples with different powder ratios, demonstrating that the D4 (80:20) sample exhibits optimal performance. This formulation achieves a flexural strength of 823 MPa, representing a 16% improvement compared to the D1 (100:0) sample. Comprehensive mechanical characterization reveals concurrent enhancements in other properties, including an elastic modulus of 208 GPa and Vickers hardness of 14.4 GPa.

Fig. 13 presents the mechanical properties of five samples with optimal composition (80:20) sintered at different temperatures. The results demonstrate that the sample sintered at 1550°C exhibits optimal mechanical performance.

Fig. 14(a) illustrates the influence of different powder size ratios on transmittance at 1550°C, measured at the characteristic wavelength of 600 nm. The selection of 600 nm for transmittance testing in zirconia ceramic research, particularly for dental restorative materials, is based on comprehensive considerations of industry standards, human visual characteristics, and material optical properties. The results reveal that transmittance first increases and then decreases with increasing fine powder content, with the D4 (80:20) sample achieving an optimal transmittance value of 48.9%. However, the excessively high viscosity of the D5 (70:30) slurry prior to sample preparation causes deterioration in printing quality, leading to reduced transmittance. Fig. 14(b) shows the transmittance variations of D4 (80:20) samples at different sintering temperatures. The specimen sintered at 1550°C reaches peak transmittance. Further increasing the temperature to 1600°C reduces transmittance due to abnormal grain growth.

Table 2 presents systematic comparative test data of samples with five powder ratios sintered at 1550°C. Under a solid loading of 45 vol%, the D4 (80:20) sample exhibited a viscosity of 4.94 Pa·s at 50 s^{-1} shear rate with a curing depth of 165 μm, meeting DLP printing requirements. The comprehensive performance was simultaneously enhanced, demonstrating a flexural strength of 823 MPa, elastic modulus of 208 GPa, Vickers hardness of 14.4 GPa, and transmittance of 48.9% at 600 nm wavelength. Experimental results indicate that particle size distribution affects the rheological and curing properties of the slurry, while also influencing the mechanical properties and transmittance of sintered samples. A moderate increase in fine powder content can effectively enhance the mechanical properties of the material; however, when the fine powder addition becomes excessive, the sharp rise in slurry viscosity will lead to deteriorated printing quality of zirconia ceramics, consequently adversely affecting their overall performance.

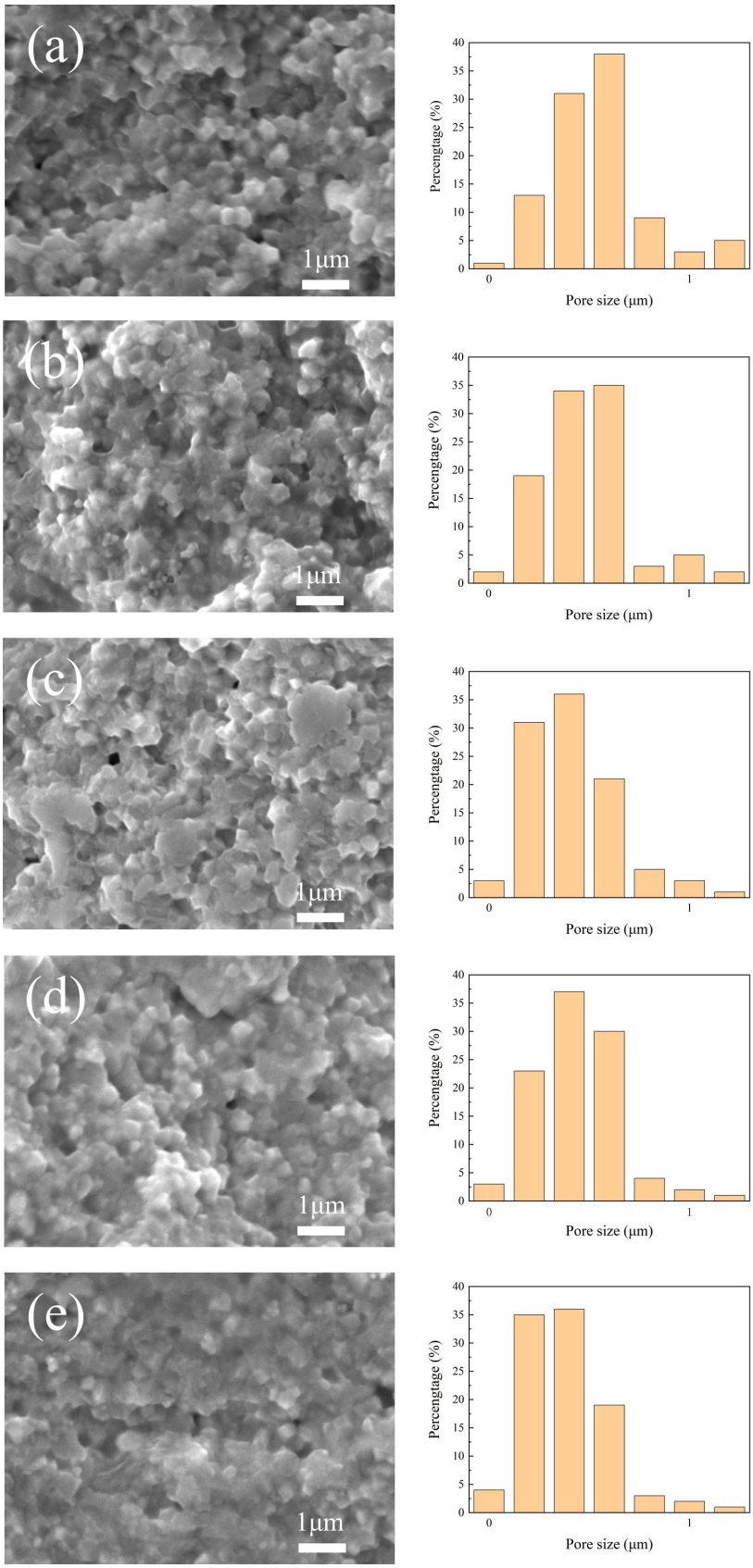

Figure 8. SEM fracture images of samples with different ratios sintered at 1550°C: (a) D1 (100:0), (b) D2 (95:5), (c) D3 (90:10), (d) D4 (80:20), (e) D5 (70:30).

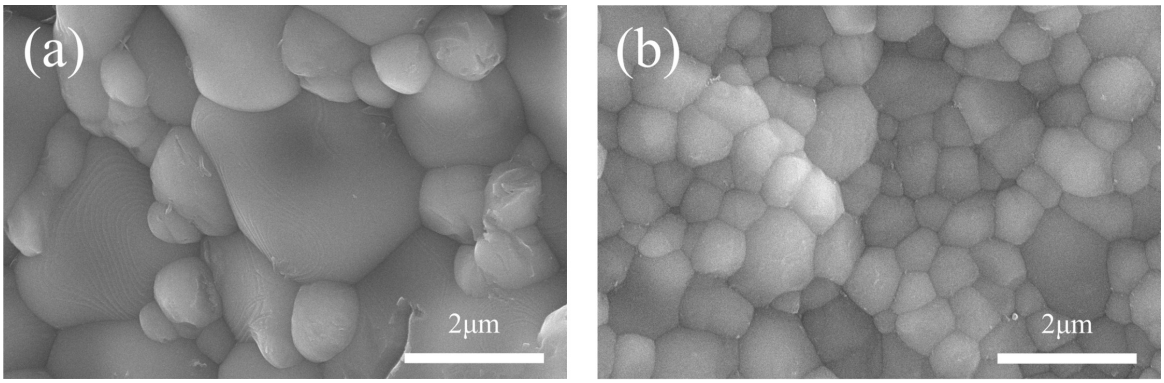

Figure 9. (a) Surface groove SEM image of D1 (100:0) sample sintered at 1550°C, (b) Surface groove SEM image of D4 (80:20) sample sintered at 1550°C.

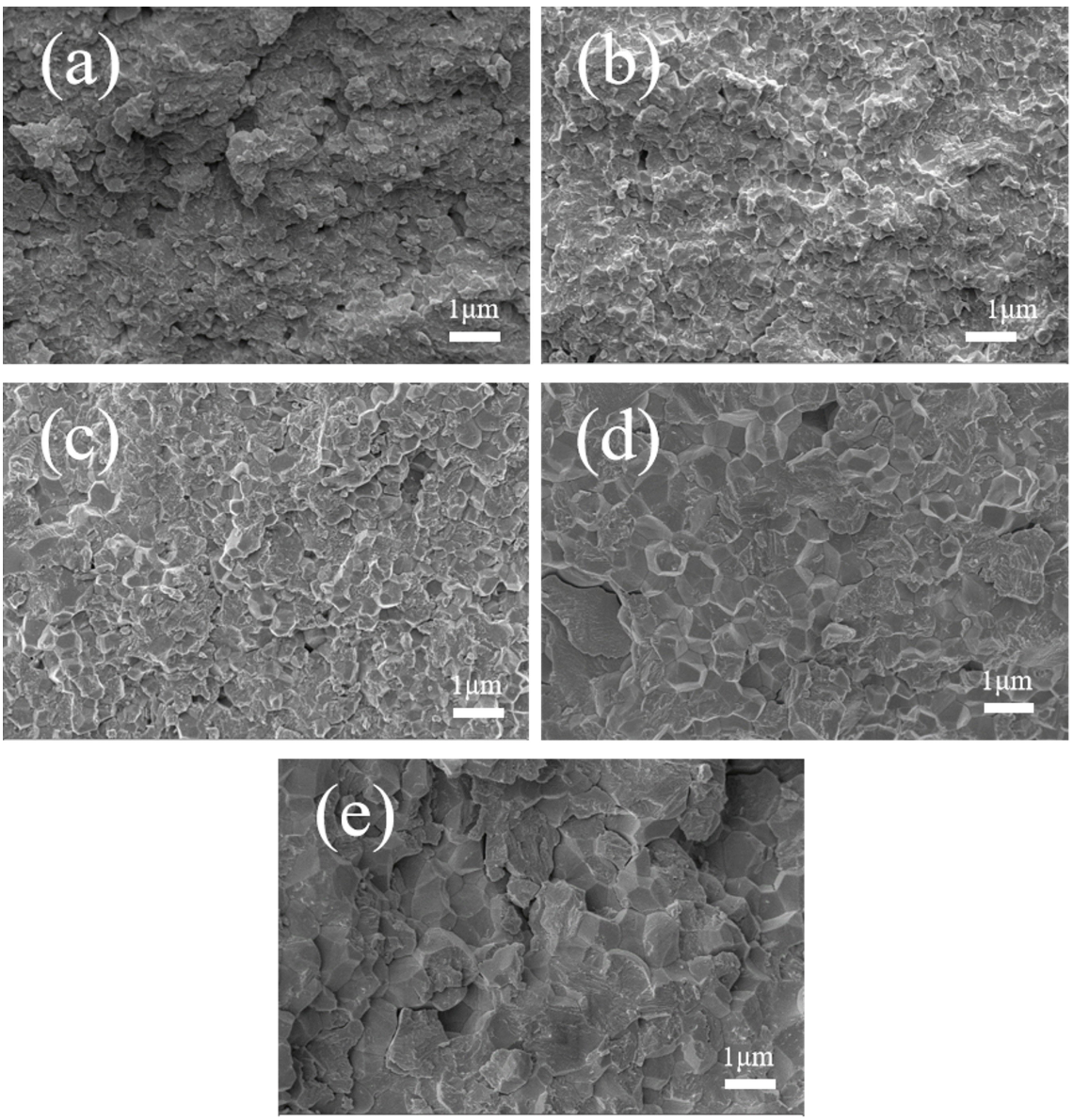

Figure 10. Fracture surface SEM images of D4 (80:20) samples sintered at different temperatures: (a) 1400°C, (b) 1450°C, (c) 1500°C, (d) 1550°C, (e) 1600°C.

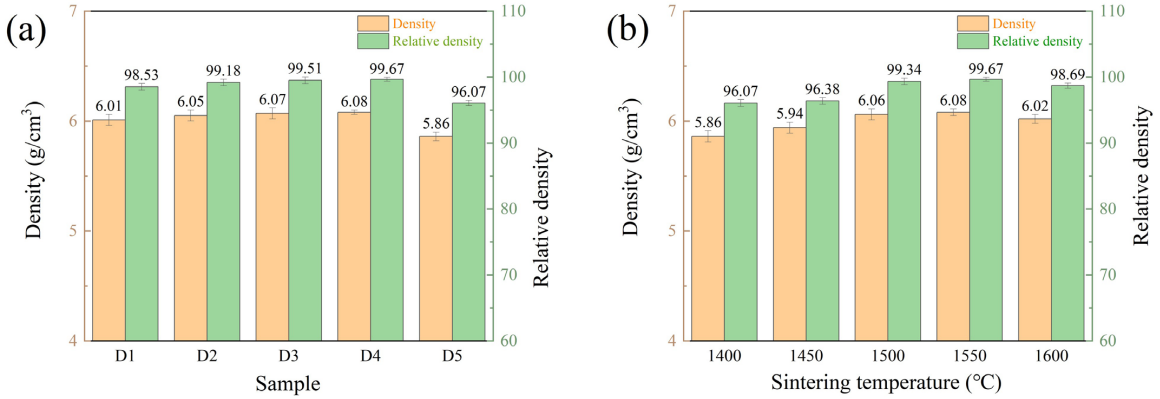

Figure 11. (a) Density and relative density of zirconia with different ratios sintered at 1550°C, (b) Density and relative density of zirconia with D4 (80:20) ratio at different sintering temperatures.

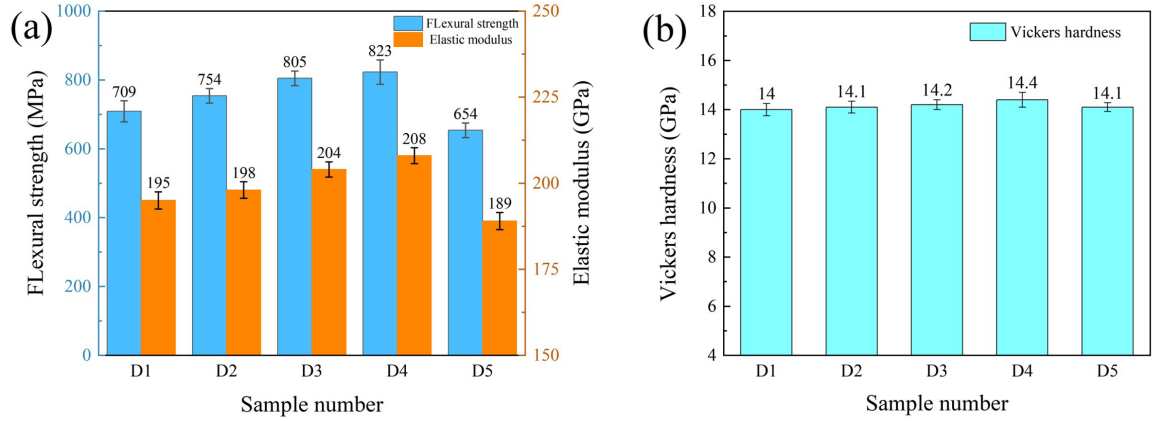

Figure 12. (a) Flexural strength and elastic modulus of 1550°C-sintered samples with different composition ratios, (b) Vickers hardness of 1550°C-sintered samples with different composition ratios.

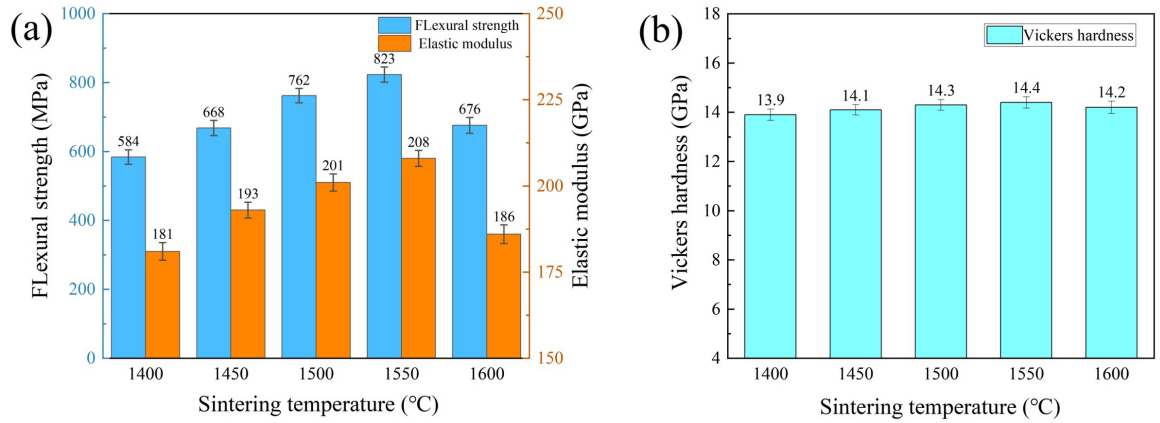

Figure 13. (a) Flexural strength and elastic modulus of D4 (80:20) samples at different sintering temperatures, (b) Vickers hardness of D4 (80:20) samples at different sintering temperatures.

As shown in Table 3, systematic characterization of D4 (80:20) samples prepared at different sintering temperatures yielded the following comparative results: the specimen sintered at 1550°C demonstrated the best overall performance.

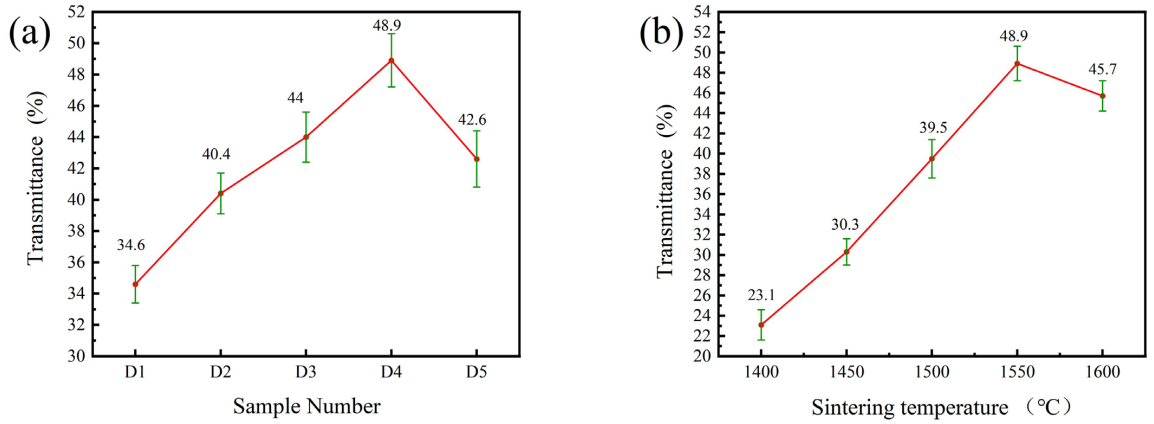

Figure 14. (a) Transmittance of samples with different ratios sintered at 1550°C at the characteristic wavelength of 600 nm, (b) Transmittance of D4 (80:20) samples at different sintering temperatures at the characteristic wavelength of 600 nm.

Table 3. Comparison of mechanical properties of ZrO_2 ceramics at different sintering temperatures.

Temperature (°C)	Density (g/cm^3)	Flexural strength (MPa)	Elastic modulus (GPa)	Vickers hardness (GPa)	Transmittance **(%)**
1400	5.86	584	181	13.9	23.1
1450	5.94	668	193	14.0	30.3
1500	6.06	762	201	14.3	39.5
1550	6.08	823	208	14.4	48.9
1600	6.02	676	186	14.2	45.7

4. Conclusion

Through particle gradation optimization, DLP-fabricated zirconia ceramics achieved overall performance enhancement. Although the introduction of fine powders increased slurry viscosity while their expanded specific surface area improved UV absorption efficiency—resulting in reduced cure depth, both mechanical and optical properties were improved. Among the five formulated ratios, the D4 (80:20) powder ratio demonstrated optimal comprehensive performance, with its slurry exhibiting a viscosity of 4.94 Pa·s at 50 s^{-1} shear rate and achieving a cure depth of 165 μm at 120 mJ/cm^2 exposure energy. Systematic investigation across the 1400-1600°C sintering temperature range confirmed 1550°C as the optimal sintering temperature. At this temperature, the sintered bodies achieved a relative density of 99.67% and reached a flexural strength of 823 MPa, representing a 16.08% enhancement compared to D1 (100:0) samples. Both elastic modulus and Vickers hardness showed improvements, reaching 208 GPa and 14.4 GPa respectively, while the transmittance increased to 48.9% at 600 nm wavelength.

5. Acknowledgments

The authors appreciate the financial support from the Shandong Provincial Natural Science Foundation (No. ZR2019MEM055; The National Natural Science Foundation of China (No. 51872118);Shandong Provincial Key Research & Development Project (NO2024CXPT018).

6. References

1. Preis V, Behr M, Hahnel S, Handel G, Rosentritt M. In Vitro failure and fracture resistance of veneered and full-contour zirconia restorations. J Dent. 2012;40(11):921-8. https://doi.org/10.1016/j.jdent.2012.07.010. PMid:22835417.
2. Miyazaki T, Nakamura T, Matsumura H, Ban S, Kobayashi T. Current status of zirconia restoration. J Prosthodont Res. 2013;57(4):236-61. https://doi.org/10.1016/j.jpor.2013.09.001. PMid:24140561.
3. Duraccio D, Mussano F, Faga MG. Biomaterials for dental implants: current and future trends. J Mater Sci. 2015;50(14):4779-812. https://doi.org/10.1007/s10853-015-9056-3.
4. Wang W, Yu H, Liu Y, Jiang X, Gao B. Trueness analysis of zirconia crowns fabricated with 3-dimensional printing. J Prosthet Dent. 2019;121(2):285-91. https://doi.org/10.1016/j.prosdent.2018.04.012. PMid:30017167.
5. Wei L, Zhang J, Yu F, Zhang W, Meng X, Yang N, et al. A novel fabrication of yttria-stabilized-zirconia dense electrolyte for solid oxide fuel cells by 3D printing technique. Int J Hydrogen Energy. 2019;44(12):6182-91. https://doi.org/10.1016/j.ijhydene.2019.01.071.
6. Christensen GJ. Choosing an all-ceramic restorative material: porcelain-fused-to-metal or zirconia-based? J Am Dent Assoc. 2007;138(5):662-5. https://doi.org/10.14219/jada.archive.2007.0239. PMid:17473046.
7. Sengupta P, Bhattacharjee A, Maiti HS. Zirconia: a unique multifunctional ceramic material. Trans Indian Inst Met. 2019;72(8):1981-98. https://doi.org/10.1007/s12666-019-01742-9.
8. Sun L, Dong P, Zeng Y, Chen J. Fabrication of hollow lattice alumina ceramic with good mechanical properties by digital light processing 3D printing technology. Ceram Int. 2021;47(18):26519-27. https://doi.org/10.1016/j.ceramint.2021.06.065.

9. Rosen D, Kim S. Design and manufacturing implications of additive manufacturing. J Mater Eng Perform. 2021;30(9): 6426-38. https://doi.org/10.1007/s11665-021-06030-6.
10. Sing SL, An J, Yeong WY, Wiria FE. Laser and electron-beam powder-bed additive manufacturing of metallic implants: a review on processes, materials and designs. J Orthop Res. 2016;34(3):369-85. https://doi.org/10.1002/jor.23075. PMid:26488900.
11. Zhang Q, Sun C, Zheng J, Wang L, Liu C, Li D. Mechanical behaviour of additive manufactured PEEK/HA porous structure for orthopaedic implants: materials, structures and manufacturing processes. J Mech Behav Biomed Mater. 2025;163:106848. https://doi.org/10.1016/j.jmbbm.2024.106848. PMid:39671975.
12. Zadpoor AA, Malda J. Additive manufacturing of biomaterials, tissues, and organs. Ann Biomed Eng. 2017;45(1):1-11 https://doi.org/10.1007/s10439-016-1719-y. PMid:27632024.
13. Lin L, Wu H, Xu Y, Lin K, Zou W, Wu S. Fabrication of dense aluminum nitride ceramics via digital light processing-based stereolithography. Mater Chem Phys. 2020;249:122969. https://doi.org/10.1016/j.matchemphys.2020.122969.
14. Mitteramskogler G, Gmeiner R, Felzmann R, Gruber S, Hofstetter C, Stampfl J, et al. Light curing strategies for lithography-based additive manufacturing of customized ceramics. Addit Manuf. 2014;1-4:110-8. https://doi.org/10.1016/j.addma.2014.08.003.
15. Hua S-B, Su J, Deng Z-L, Wu J-M, Cheng L-J, Yuan X, et al. Microstructures and properties of 45S5 Bioglass® & BCP bioceramic scaffolds fabricated by digital light processing. Addit Manuf. 2021;45:102074. https://doi.org/10.1016/j.addma.2021.102074.
16. Aktas B, Das R, Acikgoz A, Demircan G, Yalcin S, Aktas HG, et al. DLP 3D Printing of TiO2-Doped Al2O3 bioceramics: manufacturing, mechanical properties, and biological evaluation. Mater Today Commun. 2024;38:107872. https://doi.org/10.1016/j.mtcomm.2023.107872.
17. Komissarenko DA, Sokolov PS, Evstigneeva AD, Slyusar IV, Nartov AS, Volkov PA, et al. DLP 3D printing of scandia-stabilized zirconia ceramics. J Eur Ceram Soc. 2021;41(1): 684-90. https://doi.org/10.1016/j.jeurceramsoc.2020.09.010.
18. Mitteramskogler G, Gmeiner R, Felzmann R, Gruber S, Hofstetter C, Stampfl J, et al. Light curing strategies for lithography-based additive manufacturing of customized ceramics. Addit Manuf. 2014;1–4:110-8. https://doi.org/10.1016/j.addma.2014.08.003.
19. Halloran JW. Ceramic stereolithography: additive manufacturing for ceramics by photopolymerization. Annu Rev Mater Res. 2016;46(1):19-40. https://doi.org/10.1146/annurev-matsci-070115-031841.
20. Su J-J, Li X-Y, Liu Z-M, Wu J-M, Huang C, Yao C-M, et al. Mechanical and biological properties of zirconia crowns prepared by digital light processing. J Am Ceram Soc. 2025;108(6):e20452.
21. Manicone PF, Iommetti PR, Raffaelli L. An overview of zirconia ceramics: basic properties and clinical applications. J Dent. 2007;35(11):819-26. https://doi.org/10.1016/j.jdent.2007.07.008. PMid:17825465.
22. Lawn YZR. Novel zirconia materials in dentistry. J Dent Res. 2018;97(2):140-7. https://doi.org/10.1177/0022034517737483. PMid:29035694.
23. Zhang F, Reveron H, Spies BC, Van Meerbeek B, Chevalier J. Trade-off between fracture resistance and translucency of zirconia and lithium-disilicate glass ceramics for monolithic restorations. Acta Biomater. 2019;91:24-34. https://doi.org/10.1016/j.actbio.2019.04.043. PMid:31034947.
24. Jung J-M, Kim G-N, Koh Y-H, Kim H-E. Manufacturing and characterization of dental crowns made of 5-Mol% Yttria stabilized zirconia by digital light processing. Materials (Basel). 2023;16(4):1447. https://doi.org/10.3390/ma16041447. PMid:36837076.
25. Shi Z-A, Wu J-M, Fang Z-Q, Mao C, Fu L-X, Wang Q-W, et al. Particle surface oxidation modification and particle gradation strategy for the preparation of high-strength SiC ceramics via vat photopolymerization. Addit Manuf. 2024;84:104118. https://doi.org/10.1016/j.addma.2024.104118.
26. Liu Y, Zhan L, Wen L, Cheng L, He Y, Xu B, et al. Effects of particle size and color on photocuring performance of Si3N4 ceramic slurry by stereolithography. J Eur Ceram Soc. 2021;41(4):2386-94. https://doi.org/10.1016/j.jeurceramsoc.2020.11.032.
27. Zhao J, Chu W, Song T, Bi L, Liu J, Han Z, et al. Digital light processing of high-strength Si3N4 ceramics: role of particle grading on slurries curing and mechanical properties. Ceram Int. 2024;50(13, Pt A):22722-32. https://doi.org/10.1016/j.ceramint.2024.03.375.
28. Hu C, Chen Y, Yang T, Liu H, Huang X, Huo Y, et al. Effect of SiC powder on the properties of SiC slurry for stereolithography. Ceram Int. 2021;47(9):12442-9. https://doi.org/10.1016/j.ceramint.2021.01.101.
29. Olhero SM, Ferreira JMF. Influence of particle size distribution on rheology and particle packing of silica-based suspensions. Powder Technol. 2004;139(1):69-75. https://doi.org/10.1016/j.powtec.2003.10.004.
30. Essmeister J, Altun AA, Staudacher M, Lube T, Schwentenwein M, Konegger T. Stereolithography-based additive manufacturing of polymer-derived SiOC/SiC ceramic composites. J Eur Ceram Soc. 2022;42(13):5343-54. https://doi.org/10.1016/j.jeurceramsoc.2022.06.021.
31. Griffith ML, Halloran JW. Freeform fabrication of ceramics via stereolithography. J Am Ceram Soc. 1996;79(10):2601-8. https://doi.org/10.1111/j.1151-2916.1996.tb09022.x.
32. Chartier T, Chaput C, Doreau F, Loiseau M. Stereolithography of structural complex ceramic parts. J Mater Sci. 2002;37(15):3141-7. https://doi.org/10.1023/A:1016102210277.
33. Chen H, Pan Y, Chen B, Li J, Gui Z, Chen J, et al. Fabrication of porous aluminum ceramics beyond device resolution via stereolithography 3D printing. Ceram Int. 2023;49(11):18463-9. https://doi.org/10.1016/j.ceramint.2023.02.218.

Data Availability

All data supporting the findings of this study have been published within the article itself